Corrosion and hydrogen permeation in H2S environments with O2 contamination – Part 3: the impact of acetate-buffered test solution chemistry

Gaurav Joshi, Martien Duvall Deffo Ayagou, Christophe Mendibide, Thi Tuyet Mai Tran, Bernard Tribollet, Jean Kittel

Corrosion and hydrogen permeation in H_2S environments with O_2 contamination – Part 3: the impact of acetate-buffered test solution chemistry

Gaurav R. Joshi, [‡]* Martien Duvall Deffo Ayagou,** C. Mendibide,** Thi Tuyet Mai Tran,*** Bernard Tribollet*** and Jean Kittel*

[‡]Corresponding author: Gaurav R. Joshi (Gauroba@gmail.com)

* IFP Energies Nouvelles, Rond-point de l'échangeur de Solaize BP3, Solaize, F-69360 (FRANCE)

** Institut de la Corrosion Site de Saint-Etienne, ZA du parc secteur Gampille, Fraisses, F-42490 (FRANCE)

*** Sorbonne Université, CNRS, Laboratoire Interfaces et Systèmes Electrochimiques (LISE), Paris F-75005 (FRANCE)

ABSTRACT

This paper highlights the importance of considering the magnitude of acetate (ethanoate) species concentration on corrosion and hydrogen permeation rates, important factors associated with cracking initiation in steels for sour service qualification. Materials selection relies on standards, such as NACE TM0177 and NACE TM0284, which stipulate that oxygen pollution should be avoided during testing in H_2S-containing media. The 5% NaCl test solutions in current standards are buffered using acetic acid (CH_3COOH)/sodium acetate (CH_3COONa) to fix the solution pH over long periods. In this third paper, as part of a series of articles that evaluate how oxygen entry modifies the corrosion of (and hydrogen permeation across) low alloy steel membranes in H_2S-containing solutions, we investigate the effect that changing the solution chemistry has through testing X65 steel in different concentrations of acetic acid and sodium acetate in H_2S-saturated 5% NaCl solutions, i.e. Solutions A and B (NACE TM0177-2016), and the HLP solution of NACE TM 0284-2016. Increasing the total acetic acid + acetate concentration encourages a higher average X65 corrosion rate and longer-sustained hydrogen charging flux, assigned to the cathodic reaction rate enhancement by acetic acid and the iron solubilizing effects of acetates. Introducing 300 ppb of dissolved oxygen does not push the solution pH outside of the permitted error range but increases average X65 corrosion rates and, again, helps sustain hydrogen permeation flux for longer. Through an evaluation of the surface structure and electrochemical impedance spectroscopy data, this appears to be down to an increase in the permeability and porosity of the troilite $FeS_{troilite}$ dominant scale. The HLP solution (at pH 3.5), with the highest acetic acid and acetate concentration, is the most aggressive. In this electrolyte, an iron sulfide overlayer structure is attained with an oxygen-rich inner layer between the metal substrate and a thick iron sulfide film.

KEY WORDS: *Hydrogen permeation, sulfide stress cracking, electrochemical impedance spectroscopy, acetic acid corrosion*

1 INTRODUCTION

Failure of metallic components used in sour (H_2S) gas containing upstream oil and gas operations can lead to a loss of containment and arrested production, and so, well- informed materials selection strategies are required. Selecting the test conditions for carbon and low alloy steel qualification, ranking and fitness for purpose tests for sour-service is generally done with reference to a pH(y)-P_{H2S}(x) diagram to impose relative 'levels of severity' and assess material corrosion and cracking susceptibility.[1] The two parameters of pH and hydrogen sulfide partial pressure (P_{H2S}) are afforded the most importance, although it is recognized that the choice of solution chemistry can affect the test outcome.[2] The prescribed 5% NaCl test solutions in current standards are acetic acid (CH_3COOH or HAc) + sodium acetate (CH_3COONa or NaAc) buffered to fix the solution pH over long testing periods typically lasting at least 30 days. Certain laboratory experiences have rightly led some operators and materials fabricators to be cautious about the effects of HAc and NaAc during stress corrosion cracking tests, with suggestions that the susceptibility to failure is affected by their concentration and can result in non-representative outcomes.[3,4]

The NACE A solution (0.5% HAc in 5% NaCl, saturated with 100 kPa H_2S) is commonly used for hydrogen induced cracking (HIC) and sulfide stress cracking (SSC) qualification tests, and is considered quite severe. Through the exclusive addition of HAc, the initial pH of this fluid is ~2.7. Since no conjugate base (sodium acetate) is added, this solution does not possess high buffering capacity. As a result of steel corroding in the test vessel, the pH rises to a value ranging 3.6 – 4.0 as FeS saturation is simultaneously attained. This pH instability (or rather the dependence of corrosion kinetics related basification of the solution) is seen as a drawback, and could be a source of scattering in test results. The rate of the increase in pH depends on several factors, including the ratio of the volume (V) of test solution to the metal surface (S) exposed as well as the corrosion rate. High V/S ratios lead to the slowest rises in pH.[3] As a consequence, buffered test solutions such as NACE TM0177-2016 solution B (2.5% HAc + 0.41% NaAc in 5% NaCl) or NACE TM0284-2016 HLP solution (0.93 N total acetate in 5 % NaCl) may appear to be popular choices since these solutions have enabled improved pH stability even with low V/S ratios during tests.[5] This latter property is considered to be "industrially" favorable, since more test specimens can be tested within a given volume of test solution without concerns of pH drift. However, the use of such buffered solutions has other side effects on the test results that ought to be taken into account.[3] It is recognized, for instance, that acetic acid can increase the corrosion rate of low alloy steels by decreasing the protectiveness of the sulfide or carbonate scales at the metal surface through solubilizing iron.[3; 6] The impact on hydrogen charging is not well documented, and it is one of the primary parameters of interest from the point of view of hydrogen-induced cracking and sulfide stress cracking. Practically, ambient oxygen (O_2) can pollute a test medium, through incorrect or insufficient deaeration of the test solution, a poor sealing of test reactors, the use of plastic tubing permeable to oxygen, as well a multitude of operations during the test (e.g. solution sampling, pH adjustment), as discussed in Parts 1 and 2 of this series of articles.[7; 8] Through an assessment of the results of those studies, which had been conducted in unbuffered 3.5% NaCl solutions, it is generally found that that oxygen contamination ends up decreasing the solution pH, increasing ferrite corrosion rate and limiting hydrogen uptake.

In this third paper of this series of work investigating the corrosion of, and hydrogen permeation across, ferritic steel in H_2S-containing aqueous solutions under oxygen contamination, we extend the experimental parameter space to consider the performance of a widely used alloy class (X65) in qualification standard prescribed acetate-buffered solutions. Consistent with our previous articles,[7; 8] we study the evolution of the solution pH with/without oxygen contamination during immersion testing. Simultaneously, the effect of buffer solution chemistry/O_2 contamination on X65 steel corrosion rates (through *in situ* EIS of the H-entry face and mass loss measurements) and hydrogen uptake rates (through Devanathan-Stachurski anodic extraction at the H-exit face) as a function of exposure time is examined. Surface analyses using X-ray diffraction (XRD) and scanning electron microscopy (SEM) support the discussion on the effects of buffer solution concentration and oxygen contamination.

2 EXPERIMENTAL PROCEDURES

Exposure of X65 steel specimens was carried out in a jacketed Devanathan-Stachurski type cell.[9] A sour-service grade X65 low alloy steel (conforming to API 5L / ISO 3183 requirements) with a ferritic-pearlitic microstructure was employed in this work. The solution temperature was maintained at 24 ± 1°C, through circulating thermally-controlled water through the cell's jackets. The X65 membrane was used for two distinct types of simultaneous electrochemical measurements. EIS measurements were performed at the buffered H_2S-saturated solution charging side at the free corrosion potential (E_{corr}). At the same time, the exit surface of the membrane (with a Pd electrodeposit) was held in a deoxygenated 0.1 M NaOH solution and polarized at a potential of +250 $mV_{Hg/HgO\ (1M\ KOH)}$ reference electrode providing a direct measurement of the hydrogen flux across the steel membrane. Membrane thicknesses were 0.5 mm, and the exposed area was 16.6 cm². In addition to the permeation membrane, weight-loss specimens of the same material (9 mm x 9 mm x 0.5 mm) were also introduced into the charging cell for weight-loss corrosion rate assessments and surface analysis. The relevant preparation and experimental procedures are detailed in previous articles.[7; 8] The test solution volume to total metal surface area ratio (V/S) was maintained at 30 mL/cm², as per our previous works.[7; 8] Solution convection was provided through continuous test gas bubbling at a rate of 5 mL/min. Standard acetate-buffered materials qualification test solutions specified by NACE TM0177-2016, i.e. solutions A and B, and HLP solution proposed by the High Strength Line Pipe research committee of the Iron and Steel Institute of Japan (ISIJ) at the same pH as NACE B (pH ~3.5) were used as the testing media.[10; 11] This latter solution is approved in NACE TM0284-2016. The solution acetic acid and acetate compositions for these different media are provided in Table 1, in a 5% NaCl (50 g/L) NaCl solution.

Table 1: Acetate concentration used in test solutions (T = 24°C, P_{H2S} ~100 kPa).

With regards the test gas, either pure H_2S (> 99.5% H_2S), or a pure H_2S + O_2 mixture (using a separate O_2 gas line to mix in an appropriate amount to provide a dissolved oxygen concentration $[O_2]_{aq}$ of 300 parts per billion (ppb or µg/L) by weight) were used to represent 'O_2-free' and 'O_2-polluted' testing scenarios respectively.[7] All tests were conducted at atmospheric pressure at a temperature of T = 24°C for a period of 720 h.

Several *in situ* measurements were conducted, including: 1) bulk solution pH evolution; 2) electrochemical impedance spectroscopy (EIS) at the corroding/H-entry face of the X65 steel membrane; and 3) hydrogen permeation at the H-exit face of the membrane. Post-experimental analyses of material weight-loss (corrosion), and surface investigations by scanning electron microscopy (SEM) and X-ray diffraction (XRD, CuKα source in a $\theta-2\theta$ geometry) were also carried out. Supplementary potentiodynamic polarisation experiments (E_{corr} → anodic/cathodic, at a sweep rate = 0.167 mV s^{-1}) were also carried out on Fe specimens exposed to Ar-deaerated buffered solutions, after 5 minutes immersion in an attempt to purely investigate the effects of the buffer solution concentration and steel microstructure on X65 corrosion kinetics, rather than H_2S-related or CO_2-related corrosion and filming effects. These results are presented first in the results section. A supplementary analysis on the complexating effect of acetic species on Fe^{2+} was carried out via UV-Vis spectroscopy. For this, the absorbance from solutions containing a fixed number of moles of $Fe^{2+}_{(aq)}$ (from a 5 mg/L $FeSO_4$ mother solution) and corresponding sodium chloride, acetic acid+ sodium acetate concentrations (NACE A, NACE B and HLP pH 3.5) was measured. This was done by placing cuvettes containing the test solutions and the indicator 1,10-phenalthroline, a reagent that "fixes" the Fe^{2+}concentration by encouraging a ligand formation, within a uV-Vis spectrometer and scanning across the electromagnetic spectral range of 320 – 900 nm. Since the indicator binds to only aqueous Fe^{2+}, this technique may serve to semi-quantitatively demonstrate what proportion of initially available Fe^{2+} is lost to acetate complexation (and so is undetected by absorbance-transmittance spectroscopy).

3 RESULTS

3.1 Impact of Buffer solution concentration in the absence of H_2S_{aq}: Potentiodynamic polarization

Fig. 1 presents ohmic drop corrected potentiodynamic polarization (PDP) curves of pure Fe in Ar-deaerated NACE A and B and HLP buffered solutions, for a basic evaluation on the effect of various acetic acid/acetate concentrations. Pure Fe was employed as it is largely representative (ferritic microstructure) and there was a lack of X65 steel specimens for this purpose.

[FIGURE 1]

Fig. 1 displays potentiodynamic polarisation (plotted as overpotential vs. log current density) data of Fe exposed to Ar-deaerated NACE A, B and HLP solutions. E_{corr} values are presented in Table 2. Fig. 1 includes partial anodic and cathodic current density slopes extrapolated to the intersections for a semi-quantitative comparison using dashed lines. All three datasets present similar shaped curves in the activation control at small overpotentials either side of OCP, as well as diffusion-limited (cathodic) and ohmic drop controlled (anodic) regions at larger overpotentials. A classical activation-controlled Tafel kinetics analysis is not conducted since a clear linear decade of log current density was not obtained in the anodic part of the PDP curves. The partial anodic slopes, all rather similar, were taken from a limited range of linearity (+50 mV_{Ecorr} to +120 mV_{Ecorr}), whereas the partial cathodic slopes were extrapolated from the diffusion-limited cathodic regime (potential range from -100 to -400 mV_{Ecorr}). This latter slope tends well beyond 350-400 mV $decade^{-1}$, confirming the diffusion-limitation. The near OCP activation-controlled kinetics in the anodic and cathodic regimes are overlapping, as reported by Tran *et al.*;[12] nonetheless, differences in the magnitude of the cathodic diffusion-limited current densities as a function of the total [HAc + Ac] concentration are rather distinguishable. It is interesting to note that despite having a lower pH of ~2.6 (an H^+ concentration 6 times higher than the NACE B and HLP solutions which were at pH 3.5), the cathodic ferrite kinetics in the NACE A solution were measured to be the lowest. It appears that increasing the [HAc + Ac] concentration may well increase the diffusion-limited current density at a steel surface,[12,13] and is possibly apparent from our data here. Furthermore, literature reports published in this last decade suggest that a buffering effect mechanism played by the acetic acid/acetate equilibrium, to supply protons for the cathodic reduction, might be responsible:[14; 15]

$$CH_3COOH \leftrightarrow CH_3COO^- + H^+ \qquad (1)$$

We understand that this dissociation reaction (Eq. 1) would take place in the diffusion layer or is catalyzed on contact with a cathodic reaction site at the steel or a conductive corrosion product surface. On the basis of such a mechanistic viewpoint, we consider that the cathodic reaction is most likely a diffusion-limited proton reduction reaction that is preceded by an adsorbed HAc step. It suggests that the dissociated H^+ concentration, which is more than an order of magnitude lower than the free HAc concentration, might have less of an impact on the diffusion-limited cathodic current than the [HAc + Ac] concentration in these "artificial" buffer solutions. By accepting that the intersection of the partial anodic (activation) and cathodic (diffusion-limited) slopes in Fig 1 provides an estimate for the corrosion current density (j_{corr}), we estimate the initial current densities at approximately 80, 100 and 120 µA cm^{-2} in NACE A, NACE B and HLP pH 3.5 solutions respectively. By assigning an arbitrary "corrosion factor" of 1 to the j_{corr} of Fe in Ar-deaerated NACE A solution, we note that NACE B and HLP induce corrosion currents that are ~1.33 and ~1.5 times higher respectively. Table 2 lists some evaluated parameters from the PDP assessment on Fe. It is to be stressed that these approximations on our corrosion kinetics observations suffice in highlighting the fundamental (and elsewhere-confirmed) trend that a greater concentration/activity of acetic acid + acetates should lead to higher diffusion-limited currents.[14; 15] Furthermore, as shown later in this article, these PDP data on Fe support the longer term corrosion trends observed for X65 steel over 30 days in the selected acetate-buffered, H_2S-saturated solutions.

Table 2: Potentiodynamic polarization values for Fe in the different Ar-deaerated buffer solutions (T = 24°C).

3.2 Impact of O_2 on Buffer solution pH

[FIGURE 2]

Fig. 2(a) shows the results of the pH as a function of time over 720h (P_{H2S} and P_{tot} = 100 kPa, T = 24°C) for the various test solutions. The pH profiles in the O_2 –free buffered test solutions (Fig. 2(a)) remain relatively stable around 3.5 ± 0.1. The NACE A solution, lacking in acetate ion buffering capacity, is noted to increase and eventually approach pH 3.5 from two repeats. The initial peak is assigned to the rapid basification caused by high initial corrosion rates and the stabilization is attained with the saturation of FeS-type corrosion products. For the NACE B and HLP pH 3.5 solutions, the substantial acetate ions with respect to hydrosulfide ions (HS^-) in this solution, brings about the pH stability through HAc/Ac buffering and not the H_2S/HS^- weak acid buffer. Fig 2(b) presents the pH evolution profiles in the oxygen-polluted scenarios, where H_2S and O_2 gas are constantly renewed in the test solutions through gas bubbling. Unlike the unbuffered NaCl solution reported in previous articles from this research programme,[7; 8] where a continuous acidification is clearly observed, the acetate-buffered solutions contaminated by oxygen exhibit a very little difference compared to their respective O_2-free solutions, and remain within the desired pH range specified by NACE TM0177. The O_2-contaminated NACE A solution does present a downward trajectory and suggests some acidification, possibly because of a weaker buffering capacity with respect to NACE B and HLP pH 3.5. If the solution chemistries are considered, including the dissolved concentrations at equilibrium and the partial pressures of both gases, $[H_2S]_{aq}$ is always in far greater excess compared to 300 ppb $[O_2]_{aq}$ (concentrations of ~0.1 M and ~0.01 M respectively). The bubbled O_2 dissolves in solution and is understood to react with H_2S_{aq} to acidify the solution [7,16; 17].

$$2H_2S_{(aq)} + 2O_{2\,(aq)} \rightarrow S_2O_3^{2-}{}_{(aq)} + 2H^+{}_{(aq)} + H_2O_{(l)} \qquad (2)$$

The instability of thiosulfate anions means they would then oxidize to form more stable sulfates anions and elemental sulfur, i.e.

$$S_2O_3^{2-}{}_{(aq)} + \tfrac{1}{2}\,O_{2\,(aq)} \rightarrow SO_4^{2-}{}_{(aq)} + S \qquad (3)$$

As acetate ions consume the produced acidity, the weak acid/conjugate base equilibrium in Equation 1 shifts slightly to the left. This has the general effect of decreasing the available acetate ion concentration for buffering, and ever so slightly decreasing the solution pH. The acetate/acetic acid pH buffer (NACE B and HLP) serves to limit any cumulative acidification, which is suffered by the unbuffered O_2-contaminated 3.5% NaCl solution in previous works.[7] The acetate buffering restricts the solution pH to the required range during standardized testing.[10] In that regard, assessing the *in situ* pH may not be a reliable indicator of a potential oxygen contamination in acetate-buffered solutions during qualification testing.

3.3 Impact of Buffer solution chemistry on corrosion

3.3.1 De-aerated solutions

Fig. 3 shows Nyquist impedance data, after short (2 days) and long (25 days) exposure times, taken from the H-entry surface, exposed to the H_2S–saturated buffer solution, for the O_2-free and O_2-contaminated systems. In Fig. 3(a), the values of X65 charge transfer resistance (proportional to the semicircle diameter in the Nyquist complex plane format) are greater after 25 days of exposure if compared against the value measured after 2 days. This type of result is typically associated with a decrease of corrosion rate and the formation of a protective scale. The same effect is seen in the NACE B solution (Fig 3(c)), albeit to a smaller extent. This is not the case for X65 in the HLP solution, where we observe comparable Nyquist semicircles at short and long immersion times (Fig. 3 (e)). In all the O_2-contaminated solutions (Fig. 3 (b,d and f)), the magnitude of the Nyquist semicircle is always lower after 25 days exposure, indicative of an aggravation of the corrosion rate.

[FIGURE 3]

In order to verify the number of time constants, a Bode representation after subtracting the electrolyte resistance is shown in Fig. 4, using the short term NACE A data as a representative example. From this figure, we can see that the high frequency measurements above 100 Hz become quite noisy, i.e. the contribution of the HF capacitance is negligible relative to the electrolyte resistance. A similar behavior has been presented in a previous article related to EIS analysis of pure iron exposed to H_2S solution[23]. This high frequency perturbation is associated with the contribution of a conductive and highly porous iron sulfide film, which results in atypically high interfacial scale capacitances. We note that below 100 Hz, the Phase angle representation shows only one time constant (10 Hz – 10 mHz range), which we attribute to the charge transfer resistance (R_{ct}) in parallel to the double-layer capacitance (C_{dl}). This is later validated against the mass loss corrosion rates and shown to be a reasonable approach.

[FIGURE 4]

Modeling the EIS data is detailed elsewhere,[18] and was performed using SIMAD® software developed by the LISE laboratory (Sorbonne University, Paris). For the purposes of the present article, we believe it is sufficient to calculate the charge transfer resistances (R_{ct}) and effective double layer capacitances (Eff C_{dl}), from the Randles equivalent circuit model for corrosion rate calculations. Extracted EIS data at short and long exposure times are summarized in Table 3. This approach is valid since only one clear time constant is obtained for the vast majority of acquired

data. As already shown in our previous article,[18] FeS scales cause extremely high values of the effective double layer capacitance. This is also the case here irrespective of the acetate content.

Table 3: Extracted EIS parameters for X65 at short (2 days) and long (25 days) exposures to O_2-free and O_2-contaminated buffer solutions (T = 24°C, P_{H2S} ~100 kPa).

The evolution of corrosion rates (CR) is derived from Eq. 4 and 5, and presented in Fig. 5(a) (assuming b_a , the anodic Tafel coefficient = 0.04 V/dec). The justification behind this approach is explained in Ref [18], where the impedance for Fe in H_2S_{aq} is shown to be dominated by the anodic reaction process.

$$j_{corr\ (A\ cm^{-2})} = b_{a\ (V/decade)} / 2.3\ R_{ct\ (\Omega\ cm^2)} \quad (4)$$

$$CR_{(\mu m\ yr^{-1})} = j_{corr\ (\mu A\ cm^{-2})} \times MC_{Fe} \quad (5)$$

In Eq. (5), MC_{Fe} = Fe material constant (1.17×10^7 µm cm² A^{-1} yr^{-1} for Fe corrosion to Fe^{2+} and takes into account the unitary conversions, the number of seconds in a year, Fe atomic weight, steel density, the mol of e^- transferred per mol of Fe (2) and Faraday's constant).

[FIGURE 5]

Table 4 Comparisons of mass-loss corrosion rates and integrated electrochemical corrosion rates (EIS CR) of X65 samples after exposure to O_2-free and O_2-contaminated buffer solutions (T = 24°C, P_{H2S} ~100 kPa) for a period of ~30 days.

The electrochemical corrosion rate data are supported by coupon mass loss corrosion rates (Table 4). An acceptable correlation is obtained between mass loss and integrated electrochemical impedance spectroscopy corrosion rate estimates for the oxygen-free systems throughout the testing campaign, which justifies the choice of b_a ~ 0.04 V/dec as the Stern-Geary coefficient. Nonetheless, average weight-loss corrosion rates in the presence of O_2 happened to be slightly higher on average with respect to the EIS estimates. Focusing on X65 performance in O_2-free solutions, it is noted that the shapes of the CR profiles (Fig. 5 (a)) in NACE solutions are quite similar but their magnitudes vary. X65 corrodes at a higher rate in NACE B relative to NACE A, before both CRs decrease to low values over the final 15 days of immersion (to a CR that is ~90% lower than its value recorded on day 15). The CR in the HLP pH 3.5 solutions is maintained at the highest rates amongst the O_2 free solutions, and presents a slower rate of decrease over the final 15 days of immersion (a final CR that is only 30% lower than its value recorded on day 15). Such profiles lend themselves to the hypothesis that well protective overlayers are formed in the NACE solutions before the 30th day of exposure but a semi-protective one, at best, forms in the HLP pH 3.5 solution. For these H_2S-saturated acetate-buffered NaCl solutions under the same partial pressure (100 kPa), the same solution H_2S concentration (~0.1M H_2S_{aq}), the same solution pH (3.5 ± 0.2) and comparable hydrodynamics, it is the higher HAc + Ac concentration that elevates the base CR (i.e. HLP pH 3.5 > NACE B > NACE A). Such an effect has been confirmed elsewhere in the literature.[11] As discussed earlier, we assign this to an increase in diffusion-controlled cathodic reduction kinetics resulting from a higher acetic acid concentration. However, over long exposure times, the higher acetate anion concentration possibly also plays an important role through competitive specific ion interaction and complexation with ferrous ions to form aqueous iron acetate $Fe(CH_3COO)_2$ rather than solid iron sulfide precipitates (Fe_xS_y).[6] The former species remains dissolved due to its higher solubility in aqueous media relative to iron sulfides. The metal loss corrosion reactions in these H_2S-saturated acetate-buffered media, that we suspect are most relevant, are provided in Equations (6-9). [19]

$$Fe + H_2S_{aq} \rightarrow FeS_{(s)} + 2H_{ad} \quad (6)$$

$$Fe + CH_3COOH \rightarrow Fe(CH_3COO)_{2\ (aq)} + 2H_{ad} \quad (7)$$

$$Fe^{2+} + 2CH_3COO^- \rightarrow Fe(CH_3COO)_{2\ (aq)} \quad (8)$$

$$Fe(CH_3COO)_{2\ (aq)} + H_2S_{aq} \leftrightarrow FeS_{(s)} + 2\ CH_3COOH \quad (9)$$

In this manner, acetate anions might sustain substrate corrosion through disrupting the development of protective iron sulfide, whereas a higher acetic acid concentration drives a higher mass-transfer controlled cathodic reaction and participates in dissolving existing Fe_xS_y (reverse of Equation 9). We expect that these phenomena combine to elevate the baseline CR in the HLP pH 3.5 solution, relative to the NACE solutions. In an effort to observe the solubilizing/complexation effect of acetic acid + sodium acetate on Fe^{2+}(aq), Fig. 6 presents uV-Vis data from 5 solutions containing, ostensibly, the same Fe^{2+} concentration of 5 mg/L (from a $FeSO_4$ mother solution), namely (a) deionized water, (b) 5% NaCl,(c) NACE A

(0.5% CH_3COOH+5%NaCl), (d) NACE B (0.41% CH_3COOH + 2.5wt% CH_3COONa + 5%NaCl) and (e) HLP 3.5 (0.82% CH_3COOH + 5wt% CH_3COONa + 5%NaCl).

[FIGURE 6]

Examining this figure conveys that the peak absorbance for Fe^{2+} slightly decreases with the addition of NaCl (first – 5% NaCl), then acetic acid (NACE A) and finally a combination of acetic acid + sodium acetate (NACE B/ HLP pH 3.5). In two repeats of these measurements, the same trends are obtained and the absorbance peaks for NACE B and HLP are overlapping, possibly suggesting that the acetate complexation effect imparted by the acetate species is limited by the total dissolved iron concentration (which is quite low compared to the total acetate concentrations – see Table 1).

3.3.2 Impact of O_2 entry on corrosion

Reference to Fig. 5 shows that the H_2S-saturated acetate-buffered solutions polluted with gaseous O_2 to impart a solution $[O_2]_{aq}$ = 300 ppb all induce an increase in CR, relative to the respective O_2-free conditions. For the HLP solutions, the average CR with O_2 pollution is approximately 1.3 times greater than the CR in O_2-free solution. The O_2-polluted NACE solutions cause X65 to corrode at an average rate that is almost 2.5 times higher relative to values in O_2-free solutions. Such a difference in magnitude is comparable to our previous work on pure iron corrosion in O_2-free/polluted unbuffered NaCl solutions,[7] although those results could be correlated to an equivalent decrease in bulk solution pH (increase in the oxidant $[H^+]_{aq}$) under O_2 ingress. In the pH 3.5 buffered solutions, the solution pH (see Fig. 2) under O_2 contamination does not drastically change. It is suspected that other effects of oxygen contamination on bulk solution chemistry and scale protectiveness are also at play. These are further investigated with the aid of hydrogen permeation data and surface characterization results.

3.4 Impact of buffer solution chemistry and dissolved O_2 on hydrogen permeation

The hydrogen permeation profiles across the 0.5mm X65 membranes in the O_2-free/O_2-contaminated H_2S-saturated buffer solutions from this study are presented in Fig. 7.

[FIGURE 7]

After the initial transient peak in hydrogen permeation (j_{peak}), attained within the first two hours of exposure (values listed in Table 5), hydrogen uptake decreases sharply. A new steady-state (j_{ss}) is reached by the 5th day of exposure and maintained for a relatively long period of the test. Table 5 summarizes important stages of the H-permeation profiles, including earliest stages (j_{peak}), the steady states (j_{ss}) and the final value after 28-30 days of exposure (j_{final}).

Table 5: Important periods during H-permeation testing for X65 steel exposed to O_2-free and O_2-contaminated buffer solutions (T = 24°C, P_{H2S} ~100 kPa over 25 – 30 days exposure).

The high j_{peak} is a result of the high hydrogen concentration gradient that is very quickly established across the X65 steel sample in these media. Such an enormous peaked profile response (note how the value of j_{peak} is 3-4 times greater than the value of j_{ss}) is likely due to very little restriction to hydrogen entry via low H-re-combinative desorption kinetics, a high initial concentration of H_{ad} through the low pH and high HAc concentration, fast H-absorption kinetics and the absence of protective surface films during the earliest stages of exposure. Table 5 lists how j_{peak} in the permeation data appears to increase as a function of total acetic acid + acetate concentration, despite differences in initial pH between NACE A (pH = 2.7) and NACE B/HLP (pH = 3.5) solutions. This observation of higher current with higher total [HAc+Ac] follows the earlier extrapolations of the potentiodynamic polarisation data presented in Fig. 1. A similar ratio of the "relative corrosion factor" from Table 2 is also identified for the j_{peak} hydrogen permeation currents in the different buffered solutions; this gives weight to the hypothesis that j_{peak} is a function of the initial corrosion current density / corrosion rate (which is controlled by the cathodic hydrogen production reaction rate). It is clear that the more concentrated [HAc + Ac] solutions drive the higher diffusion-limiting cathodic corrosion current which correlates to the early-stage hydrogen uptake current.

With time, the high hydrogen *charging* (H-uptake) flux, on the same order as the hydrogen *diffusion* flux across a 0.5 mm thin steel membrane (under surface reaction control),[20; 21] is diminished to a lower but steady state value through the depletion of subsurface H_{ad} at the entry face. The flatter hydrogen steady state permeation rate (j_{ss}) profiles clearly observed between the 5th and 15th day of immersion are a balance between Fe_xS_Y (and other) corrosion product formation at the entry face (to restrict H-uptake) as well as the instantaneous cathodic reaction rate (permitting H-uptake), and is within a similar range in all buffered solutions (55 ± 5 μA/cm^2). It is not surprising that these curves are within a similar permeation current density range, since the extent of reversible and irreversible H-trapping in the material bulk is expected to be identical. This observation of similar H-permeation rates in all cases is also likely indicative of rate-*limiting* hydrogen absorption kinetics for this particular combination of steel microstructure, surface state, membrane thickness and solution volume/surface area ratio. Within this range, we find that average H-permeation rates in the O_2-contaminated buffered solutions (~58 μA/cm^2) are slightly greater than those in O_2-free conditions (~52 μA/cm^2), but not as vastly superior as the differences in the average measured corrosion rates.

Over the final 15 days of exposure, the H-permeation profiles for X65 in the O_2-free buffer solutions follow marked decreases to approximately zero current (see NACE A and B profiles) or the onset of a decrease (see HLP pH 3.5 profile). It suggests, for these cases, that

hydrogen absorption becomes restricted for the same reasons as the instantaneous CR decrease. Parts 1 and 2 of this series of articles,[7; 8] report that pure Fe corrosion rates in O_2-contaminated solutions (after a period of steady corrosion) began to increase, whilst the uptake/permeation of hydrogen across membranes significantly decreases. This had been concluded as being due to the action of corrosive non-hydrogenating cathodic electrochemistry, i.e. through the deleterious effects of thiosulfate anions,[22] or elemental sulfur formation.[23] In the present study, however, the hydrogen permeation fluxes for O_2-contaminated buffered systems are noted to mostly remain at their steady state values (day 5 – 15) even though instantaneous corrosion rates continuously increase from the 5th day of exposure. Thus, in these buffered O_2-contaminated solutions, a superior hydrogen entry is maintained at the corroding interfaces. This observed trend is totally opposite to the situation obtained for pure Fe in O_2-polluted H_2S-saturated unbuffered 3.5% NaCl exposure.[12] A clear decrease in the H-permeation current density was observed in that case.

The comparative analysis of corrosion current densities (j_{corr}) and hydrogen permeation current densities (j_{perm}) has previously allowed us to calculate the permeation efficiency (E_{perm}), which is defined as the ratio between j_{perm} and j_{corr}. It is a simple analysis that permits one to assess what extent the cathodic corrosion current density contributes to the absorbed hydrogen permeation current density (via exit face hydrogen oxidation measurements). In previous work on high purity Fe in O_2-free unbuffered H_2S-saturated NaCl solution, permeation efficiencies of ~ 100 % were attained throughout the test period of 25-30 days exposure.[12] For such a perfect correlation, there are certain requirements that need to be met, including (1) a highly efficient H-oxidation at the exit face (2) very little hydrogen trapping in the membrane bulk (3) an unimpeded hydrogen uptake at the entry face and (4) a corrosion current that is exclusively controlled by the cathodic reaction rate. We argue, qualitatively, that these conditions were largely met for a Pd-coated high purity Fe microstructure.[12] In the presence of oxygen, a decreasing permeation efficiency is noted as corrosion rates rose and hydrogen permeation rates fell. This was attributed to the increasing contribution of non-hydrogen charging cathodic charge transfer processes.

In order to remain relevant to such previous analyses, we present a similar approach in in Fig. 8 for the Pd-coated X65 steels in acetate-containing solutions from this study. Without O_2 contamination (Fig. 8 (a)), NACE A and B solutions exhibit relatively stable values of E_{perm}, fluctuating between 55 and 65 % in NACE A and between 40 and 55 % in NACE B solution, before both rise towards 100%. This rise in the final stages corresponds to the causality between corrosion and hydrogen permeation, and that is because both H-permeation and corrosion slow down during a similar exposure period. The results obtained in HLP solution are slightly different, with a continuous decrease between 40 % at short immersion times and down to 20 % after 30 days. Visually, the average E_{perm} values decrease with an increase in acetate species concentration (see day 5 – 15) because - for the same hydrogen permeation current - the HLP solution is more corrosive than the NACE solutions. It demonstrates that the corrosion rate is not exclusively controlled by an H_2S-buffered proton reduction mechanism. Rather, another charge-transfer controlled step involving the acetate species is involved. Its nature could be anodic (iron solubilizing), or cathodic but non-hydrogen charging. In addition, this X65 steel microstructure presents some H-trapping sites within the steel and a rather ineffective hydrogen uptake is highly influential through what we later confirm as extensive corrosion product formation (see surface characterization results).

[FIGURE 8]

In O_2-contaminated solutions (Fig. 8 (b)), a shallower decrease of E_{perm} is observed, as before in unbuffered solutions.[7; 8] Nonetheless, in previous cases, the corrosion current rises as the hydrogen permeation current falls. Here, a high hydrogen flux compared to O_2-free conditions (Fig 7) is simply maintained as the steel suffers a continuous increase in the corrosion rate. To offer additional insight, we probe the composition and structure of the corrosion product overlayers in the following section.

3.5 Impact of O_2 and Buffer solution on interfacial scale development

Fig. 9 presents XRD and surface SEM characterization data from exposed X65 specimens. XRD was conducted using a θ-2θ geometry using the large disc shaped hydrogen permeation membrane (diameter = 4.6 cm) as the surface of study. For these measurements, it was ensured that the X-ray beam footprint remained within the limits of the corroded surface.

[FIGURE 9]

For the NACE A solution (Fig 9 (a-c)), troilite is detected on the X65 surface exposed to the O_2-free solution, and a mixture of troilite and mackinawite for the O_2-contaminated solution. SEM images depict beam-shaped and hexagonal crystals, both being forms that can be assigned to troilite.[24] For the steel surface exposed to H_2S-saturated NACE B solution (Fig 9 (d-f)), XRD only detects troilite for the O_2-free solution; conversely, the O_2-contaminated NACE B surface had traces of pyrite in addition to the majority troilite. Rickard and co-workers have previously reported that the development of pyrite involves interplay between mackinawite, $Fe^{2+}_{(aq)}$ and polysulfides (S_n, where n = 2-8).Cliquez ici pour taper du texte.[25; 26] Polysulfides in particular are known to form in O_2-contaminated H_2S solutions,[27] which we speculate have participated in the pyrite-forming mechanism. In Fig. 9 (d-f), the O_2-free NACE B solution exposed samples are largely comprised of beam-shaped and wire-shaped crystals, rather like in the NACE A solution, ascribed to troilite.[24] We observe that although the crystal morphologies from both the NACE B solution-exposed surfaces are quite similar, the oxygen-polluted system results in iron sulfide scales that are slightly less homogeneous than their O_2-free counterparts (possibly poorly adhered crystals). One interpretation that we derive from the XRD diffractograms in Fig. 9 (d) is that through measuring intense diffraction lines from the α-Fe (from the underlying X65 steel substrate), the oxygen-containing NACE B solution iron sulfide scale is laterally inhomogeneous, and/or one with a significant porosity that permits the passage of X-rays corresponding to the steel substrate's diffraction planes.

Focusing next on the X65 steel surfaces exposed to the HLP pH 3.5 solutions (Fig. 9 (g-i)), a troilite-rich scale with minor traces of mackinawite is observed. The structure of the corrosion product scale here is quite different compared to those from the NACE solutions and comprises distinctly acicular and flower-shaped morphologies of troilite, as observed by Singer *et al.*[28] The O_2-contamination of this solution imposes a disruptive effect on scale development in the HLP solution, as evidenced from the diffraction pattern and SEM image. Although acicular and flower-like troilite morphologies are still present in Fig. 9 (i), with smaller diffuse crystals, there are flatter regions that lack coverage with crystallographic structures. The surface scale in Fig. 9(i) is less homogeneous than the surface in Fig. 9(h). The corresponding X-ray diffractogram detects a cocktail of iron sulfides comprising troilite, pyrrhotite and mackinawite as well as pyrite and its polymorph marcasite. Capturing such a mixture of unstable iron sulfides may indicate that this interface was undergoing a varying amount of solution-driven transformation processes (e.g. extensive dissolution-reprecipitation) by the 30th day of exposure.

Table 6: XRD phase IDs in (descending order of dominance) from the X65 corrosion/hydrogen permeation membrane surfaces after 30 days immersion in 100 kPa H_2S-saturated buffer solutions held at 24°C for a period of 30 days, in descending order of dominance.

The predominance of troilite as the principal corrosion product on all samples is conventionally rare,[25] but not improbable. A recent review on the topic highlights the thermodynamic stability of this phase after long term exposures of Fe to H_2S, as the "last main phase of the reaction of iron and H_2S."[24] Thus, given the high dissolved H_2S concentration (~0.1 M) and the aging time of 30 days, the detection of this iron sulfide, rather than only mackinawite, is justified. Furthermore, Liu *et al.* have observed the formation of troilite, atop mackinawite, with long aging times.[29] By comparison, the exposure of X52 to identical H_2S-saturated NACE A solution (1 bar),[30] or the exposure of pure Fe to unbuffered H_2S-saturated brine for a similar period of time only led to the development of mackinawite,[8] in line with another literature reports in similar non-buffered conditions.[31]

In order to qualitatively evaluate scale porosity and permeability as a function of acetate buffer concentration and O_2 contamination, X-ray diffraction and cross-sectional analyses on X65 were carried out. These are presented in Fig. 10, where the darkest contrast represents the cold-setting resin and the lightest contrast is the X65 metal substrate.

[FIGURE 10]

Thick Fe_xS_y overlayers that range from between 100 – 300 μm are obtained, compared to data from pure iron membranes where a 20 μm thick mackinawite layer was reported.[18] We expect that the thicker scales in the present study come about due to the higher X65 corrosion rates in the presence of acetic acid and acetates, where substrate Fe is lost to iron acetates and iron sulfides (Fe_xS_y) development. The acetate complexated iron, and the interaction of iron acetates and H_2S to reprecipitate iron sulfides (from solution), may permit their continuous growth and transformation. Focusing first on the X65 surfaces exposed to the O_2-free NACE A and B solutions (Fig. 10 (a and c)), where j_{corr} and j_{perm} were low on the 30th day, these scales appear dense and compact with isolated porous zones. The Fe_xS_y scale from O_2-contaminated NACE A solution (Fig. 10 (b)) does appear thinner in parts but not less protective than its O_2-free counterpart (Fig. 10 (a)). Nonetheless, the final corrosion rate was three orders of magnitude greater in the O_2-polluted NACE medium, with steady higher hydrogen permeation. This calls into question its protective character despite its dense appearance at this resolution and this location. The X65 surface exposed to O_2-polluted NACE B solution (Fig. 10 (d)) exposes a higher proportion of large pores and voids. The presence of gaps and roughening at the scale/X65 interface may qualitatively suggest a poor adherence, and a strong indication of undermining/under-deposit type corrosion. Turning our attention to the X65 cross-sections for the HLP solutions (Fig. 10 (e-f)), these scale/substrate interfaces appear completely different to those produced from exposure to the NACE solutions. In both cases, a darker inner layer was observed in between the lighter sulfide scale and the X65 steel. The fact that these layers were never observed in the NACE A – type solutions would indicate that their presence is related to the higher acetic acid/acetate ion chemistry in the HLP solutions. An EDS analysis was conducted to explore the nature of the inner layer, and this is presented in Fig. 11.

[FIGURE 11]

EDS mapping confirms that the majority of the scale is an iron sulfide (spectrum B). A strong OKα signal detected from the inner layer, however, indicating that this film is oxygen-rich and devoid of sulfur (with a small carbon signature). As mentioned before, the formation of aqueous iron acetate as an intermediate oxidized species (Equations 7-8) becomes more pertinent within the highest acetic acid and acetate ion concentration solutions (HLP). The high solubility of iron acetate relative to iron sulfides should ensure that it remains dissolved *in situ* during corrosion, but a fraction of this species may remain trapped at the iron/sulfide scale interface. Arguably, this could be the chemical nature of this inner scale. An alternative interpretation is that on removal and during the cross-section preparation (which involves wet polishing procedures in ambient oxygen), this inner layer oxidizes to a mixture of water-insoluble ferric (III) acetate and iron oxides. As EDS mapping is semi-quantitative at best, it is not a suitable method for conclusively determining the chemistry of this inner oxygen-rich scale. A more complete characterization of this phase (e.g. using SEM - Raman spectroscopy or TEM) was outside the remit of this work, although would certainly carry significant scientific and practical impact with regards the questions surrounding limits on solution buffer concentrations. The inner iron-carbon-oxygen containing layer does not appear to be too protective since X65 corrosion and hydrogen permeation in both types of HLP solution continue at the highest

rates. The inner layer is suspected to permit solution ingress to the metal surface, through porous/permeable channels. Another possibility is that it participates as a galvanic cathode to undermine the underlying steel and permit hydrogen uptake.

Electrochemical impedance spectroscopy permits the evaluation of the changing interface by estimating the effective double layer capacitance (Eff. C_{dl}, mF/cm^2) as a function of time. In our previous articles,[18; 32] we have applied Brug's relationship to our EIS data to derive the effective double layer capacitance from the CPE (constant phase elements):[33; 34]

$$\text{Eff } C_{dl} = [Q1\ (R_e^{-1} + R_{ct}^{-1})^{(\alpha-1)}]^{(1/\alpha)} \qquad (10)$$

Those results have demonstrated that tracking the evolution of Eff. C_{dl} can be a means of assessing the changing porosity of the evolving Fe_xS_y layer – since the large capacitance appears predominantly to be a function of the semi-conductive film's surface area. On this basis, we apply the same approach in the present article in Fig. 12 for the NACE solutions and HLP solutions, to add to the discussion on the changing interfacial characteristics.

Figure 12: Eff. C_{dl} evolution of X65 surface exposed to the buffer solutions at T = 24°C under 100 kPa H_2S over 30 days with and without O_2 contamination at ($[O_2]_{aq}$ = 300 ppb).

The Eff. C_{dl} for X65 in all solutions increases over the first 15 days of exposure to 10 - 40 mF cm^{-2}. These values are 2 to 3 orders of magnitude above conventional C_{dl} values of metals exposed to aqueous environments (100 µF cm^{-2}). As explained in a previous article, [18] this is likely related to the growing semi-conductive Fe_xS_y overlayer/different morphology crystallites with a greater volume, higher porosity and higher surface area. Focusing on the Eff. C_{dl} evolution in the O_2-free NACE solutions for the final 15 days, a decreasing effective double layer capacitance is noted that coincides well with the decreasing corrosion and hydrogen permeation rates (see Fig. 5 and 7). This observation is assigned to a decrease in the overall porosity of the surface film, leading to a less permeable and more corrosion/hydrogen uptake-resistant $FeS_{troilite}$ scale on X65 steel. The trend in the O_2-free HLP is similar, although the effective capacitance continues to rise to ~50 mF/cm² before slightly decreasing. In contrast, the Eff. C_{dl} in the O_2-contaminated NACE and HLP solutions rises throughout the exposure period to uncommonly high capacitances (70 – 120 mF cm^{-2}). It would suggest a far higher scale porosity/surface area for these overlayers, which we generally observe in SEM analysis. As the iron from the substrate X65 is lost to the iron sulfide scale, this corrosion product film undergoes continuous dissolution-precipitation reactions at the scale/solution interface over time. Under the higher acetate concentrations, we hypothesize that Fe_xS_y dissolution is enhanced but re-precipitation perhaps diminished. It leads to a highly porous and permeable structure with a high surface area. Since the Eff. C_{dl} in the O_2-polluted NACE and HLP solutions seem to continuously rise, O_2 contamination must directly or indirectly increase the porosity and permeability of the Fe_xS_y overlayer in higher acetic acid concentrations. The effective double layer capacitance in the HLP solution is also possibly lower relative to the oxygen-polluted NACE B solution through different dielectric properties offered by the inner oxygen-rich film.

4 DISCUSSION

Two clear questions that stem from the results of this study include (i) how does raising the acetic acid + acetate ion concentration change the corrosion and hydrogen permeation flux across this ferritic-pearlitic X65 material in H_2S-saturated solution ; and (ii) how and why does oxygen contamination permit corrosion/hydrogen permeation to continue at high rates in these buffered media?

With regards the first point of discussion, we observe that increasing the total [HAc + Ac] concentration/activity not only causes a higher corrosion rate, but also sustains a steady state hydrogen permeation current density for a longer period of time. As shown in Fig. 1, increasing the concentration of acetic acid + acetates, in the absence of H_2S, simply serves to increase the diffusion-controlled cathodic reaction kinetics. Over longer exposures (with H_2S_{aq}), a higher [HAc + Ac] may keep corroded Fe^{2+} in a solubilized aqueous state – complexated with acetate ions - rather than readily enabling the precipitation/formation of insoluble $FeS_{troilite}$. This is qualitatively demonstrated in Fig. 6. Indeed, the high acetic acid activity would likely dissolve existing Fe_xS_y, and reduce the overall protective ability of the scale by rendering it more porous and permeable. As long as access to the metallic surface is not too restricted by the Fe_xS_y overlayer, a supply of surface-adsorbed hydrogen for the cathodic reaction (under mass-transfer control) and the absorption of hydrogen by the X65 substrate would be assured for a longer period of time. This offers a convenient explanation for the delay in the decrease of corrosion and hydrogen permeation rates in buffered solutions as a function of acetic/acetate activities (Figs. 5 and 7), i.e. why X65 corrosion and hydrogen permeation in NACE A begins to fall rapidly after the 10th day and those in NACE B and HLP after the 15th day and 20th day of immersion respectively. In other words, the electrochemical rate-limiting (i.e. protective) capacity of Fe_xS_y bears a negative correlation with the total acetate concentration.

In *Deffo Ayagou et al*, the authors discuss how the primary effect of O_2 contamination in 100% H_2S, 3.5% NaCl at a total pressure of 100 kPa (~1 atm) is to encourage the progressive formation of thiosulfates, sulfates, elemental sulfur, and to acidify the solution as a result.[7] A rising concentration of intermediary sulfites, thiosulfates, and more stable sulfates has previously been confirmed through ionic chromatography.[8] Although using acetic buffers limits pH modification it does not prevent the production of sulfur-family reaction products. Equation 11 summarizes the reaction products of $H_2S_{(aq)}$ and $O_{2\ (aq)}$, where metastable thiosulfates produce sulfates, acidity and elemental sulfur i.e.

$$H_2S_{(aq)} + O_{2(aq)} \rightarrow SO_3^{2-} \rightarrow S_2O_3^{2-} \rightarrow SO_4^{2-} (+ 2H^+ + S_{(s)}) \quad (11)$$

The concentration of polysulfides is expected to be negligible in systems where $[O_2]_{aq}$ < 10 ppb. However, in O_2-contaminated H_2S-saturated solutions a number of pathways permit the formation of elemental sulfur, via polysulfides, sulfites, and thiosulfate disproportionation – described elsewhere.[27] Under O_2 contamination, these thiosulfates may also disproportionate into colloidal sulfur and sulfurous acid in acidic media in contact with the surface,[22] i.e.

$$S_2O_3^{2-} + 2H^+ \rightarrow S_{(s)} + H_2SO_{3\ (aq)} \quad (12)$$

$$H_2SO_{3\ (aq)} + H_2O \leftrightarrow 2H^+ + HSO_3^- \quad pKa = 1.8 \quad (13)$$

Elemental sulfur hydrolysis can contribute to reproducing H_2S, and to producing dissociated acidity and sulfates. Thus, locally, the production of such chemistries may promote the dissolution of the iron sulfide scale, and sustain corrosion and hydrogen uptake in the presence of $H_2S_{(aq)}$. Our previous work conducted under a 500 ppb O_2 contamination in 100 kPa H_2S (3.5% NaCl, T = 24°C) showed a cumulative concentration of ~100 mg/L (1 mM) of SO_4^{2-} after 25 days of exposure. The present study was conducted with a lower level of dissolved O_2 contamination corresponding to 300 ppb. On this basis, we infer that ~0.6 – 0.8 mM SO_4^{2-} may be present at the end of the test (30 day). Further, the aqueous oxidation of pyrite (a confirmed XRD corrosion product in O_2-polluted NACE B and HLP solutions) would also lead to the production of sulfate and ferrous ions. As iron sulfide crystallites undergo dissolution-precipitation, perhaps a fraction of solubilized Fe^{2+} reacts with the rising concentration of sulfates (SO_4^{2-}) and remains solubilized as iron sulfates rather than re-precipitating as iron sulfides. All such proposed phenomena may destabilize the iron sulfide film structure and increase its porosity and permeability, as interpreted from surface and cross-section characterization as well as impedance Eff. C_{dl} evolution under O_2-contamination. A porous and permeable iron sulfide scale structure would then permit the access of H_2S-saturated electrolyte to the steel interface, and sustain a high adsorbed to absorbed hydrogen equilibrium at the metal interface to ensure a high hydrogen permeation current throughout the exposure period. An exacerbation of X65 corrosion in O_2-contaminated buffer solutions may also be a result of the higher cathodic surface area contact of the porous scale to the base metal and the galvanic corrosion it encourages.[35] Even with an anodically polarised Fe surface, hydrogen entry into Fe would remain possible as long as the interfacial mixed potential (FeS/Fe oxide/Fe acetate to Fe) remains below the reversible hydrogen potential. We add that different metallurgies, e.g. bainitic or fully tempered martensitic low carbon steel, or similar metallugies with different compositions/heat treatments, may not respond in a comparable manner as the ferritic-pearlitic X65 steel from this paper. This has been demonstrated by Mendibide *et al* through their assessment of the H-permeation and cracking responses of different steel grades under O_2-polluted /removed acetate buffered solutions.[36] Qualitatively, the studied martensitic grade in that work depicts similar H-permeation flux kinetics with increasing dissolved oxygen pollution up to 300 ppb (a delay in the drop to zero current), although the absolute H-flux magnitudes are lower. There is undoubtedly significant interplay in the nature of the microstructure, interfacial filming (and stress-effects when cracking tests have been performed) that would merit further evaluation and testing.

We believe it is necessary to consider these results from a wider perspective, which could have implications for oil and gas materials qualification testing with respect to environmental cracking. The total acetic acid + acetate concentration clearly has measurable effects on hydrogen uptake/charging intensity and corrosion rates of this ferritic-pearlitic X65 microstructure in a reactor vessel with a V/S of ~30 mL/cm^2. We find that a highly protective Fe_xS_y overlayer (mainly troilite) limits further corrosion/hydrogen charging well before the end of a typically prescribed testing period of 30 days in NACE A and B solutions. Kobayashi *et al* have advocated the use of higher acetate concentrations in order to buffer the solution pH more effectively during long-term HIC qualification testing for sour-service applications.[11] Our results convey that baseline corrosion rates increase with total acetate concentration, but so do the general rates of hydrogen permeation – which are maintained at high levels throughout. It is suspected that a higher intensity of hydrogen uptake could very well induce HIC. Furthermore, we find that an artefact of using a very high acetate concentration (HLP solution) induces the formation of an inner oxygen-rich layer mixed in/beneath FeS. This HLP solution would thus appear to be an artificial and severe choice for testing materials, ideally suited to offer extremely corrosive and high hydrogen charging conditions. Under oxygen contamination, the NACE B and HLP buffers maintain the bulk solution pH within an error range prescribed by qualification standards, thus giving the impression that testing work is being carried out to the satisfactory level. However, other chemical and electrochemical effects ensure that the material corrosion/hydrogen permeation continues at devastating rates. Indeed, with highly porous overlayers and the likelihood of localised corrosion, a greater number of crack initiation sites may well lead to material fails in extremely well-buffered but O_2 compromised SSC tests.

5 CONCLUSIONS

The effect of traces of dissolved oxygen ($[O_2]_{aq}$ = 300 ppb) on the corrosion of, and hydrogen permeation across, low carbon sour-service grade X65 steel was studied in a 50 g/L NaCl test solution saturated with 100% H_2S (at P_{tot}=1 bar) containing different concentrations of acetic acid (HAc) and sodium acetate (NaAc or Ac) to represent oil and gas materials qualification testing solutions for the satisfactory buffering of test solution pH. The following conclusions are drawn from this work:

- Increasing the total acetic acid + acetate concentration encourages a higher X65 corrosion rate and longer hydrogen charging flux over 30 days;

- A decrease of *in situ* X65 corrosion rates and hydrogen uptake is noted in O_2-free solutions, but delayed to later times as a function of the total acetic acid + acetate concentration;

- Introducing dissolved oxygen increases corrosion rates and hydrogen permeation fluxes. This appears to be down to a limitation of the protective ability offered by the $FeS_{troilite}$ dominant iron sulfide scale to permit electrolyte access to the steel interface and drive the relevant electrochemical reactions for longer time.

- An oxygen-rich inner layer is identified in between the metal and iron sulfide in steel samples exposed to the highest acetates-containing solution (HLP pH 3.5), one that appears not to be too protective against corrosion or hydrogen entry.

6 ACKNOWLEDGMENTS

The authors express their gratitude to Alexandre Bonneau and Khawla Belkhadiri for their participation in the implementation of the experimental setup and acquisition of test data. We are extremely grateful to Marine Collaud and Anne-Lise Taleb from the IFP Energies Nouvelles surface characterization department for assistance with the XRD and SEM analyses.

REFERENCES

1. ISO 15156-2:2020, “Petroleum and Natural gas industries - Materials for use in H2S-containing environments in oil and gas production - Part 2: Cracking resistant carbon and low alloy steels, and the use of cast iron,” (International Organization for Standardization, 2020).
2. K. Kobayashi, T. Omura, H. Amaya, *Corrosion* 74, 7 (2018): p. 788–800.
3. J.L. Crolet, J. Leyer, “Use and abuse of artificial acetate buffering in standardized and application specific testing,” Corrosion 2004, Paper 140, March 28 - April 1 (2004).
4. Y. Ishiguro, K. Fujimura, "Choice of Buffer Solution for stainless steel OCTG Materials at Laboratory Corrosion Test to Carry Out SSC and SCC Resistance", Paper No. 9288, NACE International, Houston (TX), USA (2017).
5. “NACE TM0177-2016: Laboratory testing of metals for resistance to sulfide stress cracking and stress corrosion cracking in H2S environments,” NACE International, 2016.
6. D. Pletcher, D. Sidorin, B. Hedges, *Corrosion* 63, 3 (2007): p. 285–294.
7. M.D. Deffo Ayagou, J. Kittel, C. Mendibide, C. Duret Thual, k. belkhadiri, T.T. Mai Tran, E. Sutter, B. Tribollet, N. Ferrando, *Corrosion* 74, 11 (2018): p. 1192–1202.
8. M.D. Deffo Ayagou, G.R. Joshi, T.T. Mai Tran, E. Sutter, B. Tribollet, C. Mendibide, C. Duret-Thual, N. Ferrando, J. Kittel, *Corrosion* 75, 4 (2019): p. 389–397 (Sep. 17, 2019).
9. M.A.V Devanathan and Z. Stachurski, *J. Electrochem. Soc.* 111, 5 (1962): p. 619–623.
10. “NACE TM0374-2016: Laboratory screening tests to determine the ability of scale inhibitors to prevent the precipitation of calcium sulfate and calcium carbonate from solution (for oil and gas production systems),” NACE International, 2016.
11. K. Kobayashi, T. Omura, T. Hara, M. Okatsu, N. Ishikawa, “Proposal of HIC test solution with buffer capacity in NACE TM0284,” Corrosion 2013, 17-21 March (2013).
12. T. Tran, B. Brown, S. Nesic, B. Tribollet, “Investigation of the mechanism for acetic acid corrosion of mild steel,” Corrosion 2013, Paper 2487, 17-21 March (2013).
13. T. Hurlen, S. Gunvaldsen, F. Blaker, *Electrochimica Acta* 29, 8 (1984): p. 1163–1164.
14. A. Kahyarian, A. Schumaker, B. Brown, S. Nesic, *Electrochimica Acta* 258 (2017): p. 639–652, https://www.sciencedirect.com/science/article/pii/S0013468617324714.
15. A. Kahyarian, B. Brown, S. Nesic, “CO2 corrosion, H2S corrosion, Organic Acid Corrosion - a Unifying Perspective on Corrosion Mechanisms in Weak Acid Solutions,” Corrosion 2019, 24-28 March (2019).
16. O. Weres, L. Tsao, “Reaction of hydrogen sulfide with oxygen in the presence of sulfite: Prepared at the Earth Sciences Division at Lawrence Berkeley Laboratory, University of California,” LBL-11377, 1983.
17. Y. Song, A. Palencsar, G. Svenningsen, J. Kvarekval, T. Hemmingsen, *Corrosion* 68, 7 (2012): p. 662–671.
18. M.D. Deffo Ayagou, T.T. Mai Tran, B. Tribollet, J. Kittel, E. Sutter, N. Ferrando, C. Mendibide, C. Duret-Thual, *Electrochimica Acta* 282 (2018): p. 775–783.
19. M.A. Veloz, I. Gonzalez, *Electrochimica Acta* 48, 2 (2002): p. 135–144.
20. J. Kittel, F. Ropital, J. Pellier, *Corrosion* 64, 10 (2008): p. 788–799.
21. A. Turnbull, *Special issue on 1st International Conference on Hydrogen Storage, Embrittlement and Applications (Hy-SEA 2014), 26-30 October 2014, Rio de Janeiro, Brazil* 40, 47 (2015): p. 16961–16970, http://www.sciencedirect.com/science/article/pii/S0360319915016766.
22. L. Choudhary, D.D. Macdonald, A. Alfantazi, *Corrosion* 71, 9 (2015): p. 1147–1168.
23. G. Schmitt, *Corrosion* 47, 4 (1991): p. 285–308.
24. X. Wen, P. Bai, B. Luo, S. Zheng, C. Chen, *Corrosion Science* 139 (2018): p. 124–140 (June17, 2018).
25. D. Rickard, G.W. Luther, *Chemical Reviews* 107, 2 (2007): p. 514–562.
26. D. Rickard, G.W. Luther, *Geochimica et Cosmochimica Acta* 61, 1 (1997): p. 135–147.
27. K.Y. Chen, J.C. Morris, *Environ. Sci. Technol.* 6, 6 (1972): p. 529–537.
28. M. Singer, A. Camacho, B. Brown, S. Nešić, *Corrosion* 67, 8 (2011): 085003-1-085003-16.

29. Y. Liu, Z. Zhang, N. Bhandari, Z. Dai, F. Yan, G. Ruan, A.Y. Lu, G. Deng, F. Zhang, H. Al-Saiari, A.T. Kan, M.B. Tomson, *Ind. Eng. Chem. Res.* 56, 31 (2017): p. 9016–9027.
30. S. Zheng, C. Zhou, X. Chen, L. Zhang, J. Zheng, Y. Zhao, *Special issue on 1st International Conference on Hydrogen Storage, Embrittlement and Applications (Hy-SEA 2014), 26-30 October 2014, Rio de Janeiro, Brazil* 39, 25 (2014): p. 13919–13925.
31. P. Bai, S. Zheng, H. Zhao, Y. Ding, J. Wu, C. Chen, *Corrosion Science* 87, 0 (2014): p. 397–406.
32. M.D. Deffo Ayagou, G.R. Joshi, T.T. Mai Tran, B. Tribollet, E. Sutter, C. Mendibide, C. Duret-Thual, J. Kittel, *Corrosion Science* 164 (2020): p. 108302.
33. G.J. Brug, A. van den Eeden, M. Sluyters-Rehbach, J.H. Sluyters, *Journal of Electroanalytical Chemistry and Interfacial Electrochemistry* 176, 1 (1984): p. 275–295.
34. B. Hirschorn, M.E. Orazem, B. Tribollet, V. Vivier, I. Frateur, M. Musiani, *Electrochimica Acta* 55, 21 (2010): p. 6218–6227.
35. S.N. Esmaeely, S. Nesic, *J. Electrochem. Soc.* 164, 12 (2017): C664-C670 (Mar. 17, 2018).
36. C. Mendibide, C. Duret-Thual, M.D. Deffo-Ayagou, J. Kittel, "O2 contamination in SSC/HIC test environments. Impact on test results and discussion on acceptable limits for high H2S content," Paper 12894, 24-28 March 2019 (2019).

7 FIGURE CAPTIONS

FIGURE 1: Log *j*-E potentiodynamic polarisation (PDP) curves of pure Fe exposed to Ar-deaerated buffer solutions at T = 24°C, plotted as Log *j* vs. overpotential for comparison purposes. The E_{corr} values are listed in Table 2.

FIGURE 2: Evolution of test solution pH as a function of time over 30 days (T = 24°C, P_{H2S} = 100 kPa), (a) without and (b) with O_2 contamination.

FIGURE 3: EIS diagrams of X65 membrane at various exposure times of after 2 days and 25 days of exposure, without and with O_2 contamination ($[O_2]_{aq}$ = 300 ppb) in (a-b) NACE A (c-d) NACE B and (e-f) HLP pH 3.5 buffer solutions held at T = 24°C under 100 kPa H_2S.

FIGURE 4: EIS diagram (Bode / Phase angle plot) of X65 membrane after 2 days exposure, without O_2 contamination, in NACE A buffer solutions held at T = 24°C under 100 kPa H_2S.

FIGURE 5: Electrochemical corrosion rates of X65 membrane exposed to buffer solutions at T = 24°C under 100 kPa H_2S (a) without and (b) with deliberate O_2 contamination ($[O_2]_{aq}$ = 300 ppb).

FIGURE 6: uV-Vis spectral curves of absorbance vs. wavelength for dissolved iron (from $FeSO_4$), 4.93 x 10^{-5} ml/L, in solutions containing different concentrations of acetic acid + sodium acetate. A magnified inset is included in the top right around the peak absorbance centered at λ = 510 nm.

FIGURE 7: Hydrogen permeation across X65 membrane exposed to buffer solutions at T = 24°C under 100 kPa H_2S (a) without and (b) with deliberate O_2 contamination ($[O_2]_{aq}$ = 300 ppb).

FIGURE 8: Permeation efficiencies across X65 membrane exposed to buffer solutions at T = 24°C under 100 kPa H2S (a) without and (b) with deliberate O2 contamination ($[O_2]_{aq}$=300 ppb).

Fig. 9: XRD diffractograms and surface SEM images of X65 membranes exposed to 100 kPa H_2S-saturated (a-c) NACE A, (d-f) NACE B and (g-i) HLP buffer solutions held at 24°C for a period of 30 days. In the XRD plots, the O_2-free (black) and O_2-contaminated (red) diffractograms are presented offset.

Figure 10: Cross-sectional SEM images of X65 membranes exposed to 100 kPa H_2S-saturated (a-b) NACE A, (c-d) NACE B and (e-f) HLP pH 3.5 buffer solutions held at 24°C for a period of 30 days, with and without continuous O_2 contamination ($[O_2]_{aq}$ = 300 ppb).

Fig. 11: SEM-EDS mapping of a cross-section of X65 exposed to 100 kPa H_2S-saturated HLP buffer solution with continuous O_2 contamination (300 ppb) held at 24°C for a period of 30 days.

Figure 12: Eff. C_{dl} evolution of X65 surface exposed to the buffer solutions at T = 24°C under 100 kPa H_2S over 30 days with and without O_2 contamination at ($[O_2]_{aq}$ = 300 ppb).

8 TABLES

Table 1: Acetate concentration used in test solutions (T = 24°C, P_{H2S} ~100 kPa).

	Composition	$[HAc]_{(aq)}$ (M)	$[NaAc]_{(aq)}$ (M)	Total $[Ac^-]_{(aq)}$ (M)	initial pH
NACE A	0.5% HAc	0.08	-	0.08	2.6 – 2.7
NACE B	2.5% HAc + 0.41% NaAc	0.42	0.05	0.47	3.4 – 3.6
HLP (pH 3.5)	5.0% HAc + 0.8% NaAc	0.83	0.10	0.93	3.4 – 3.6

Table 2: Potentiodynamic polarization values for Fe in the different Ar-deaerated buffer solutions (T = 24°C).

	E ($V_{Ag/AgCl}$)	~ j_{corr} ($\mu A\ cm^{-2}$)	Rel. corr. factor
Ar-NACE A (pH 2.6±0.05)	-0.560	80	1
Ar-NACE B (pH 3.5±0.05)	-0.567	100	1.33
Ar-HLP (pH 3.5±0.05)	-0.552	120	1.50

Table 3: Extracted EIS parameters for X65 in the different buffer solutions (T = 24°C). The Effective double layer capacitance is calculated using Brug's relationship (see Equation 10 later).

			R_e (ohm cm^2)	R_{ct} (ohm cm^2)	Q1 ($ohm^{-1}\ s^{\alpha}\ cm^{-2}$)	α	Eff. C_{dl} $mF\ cm^{-2}$	χ^2	
<10 ppb O_2	NACE A	Day 2	0.02	163	2.3E-02	0.75	3	3E-02	
		Day 25	*0.02*	*4632*	*2.9E-02*	*0.71*	*3*	*6E-01*	
	NACE B	Day 2	0.02	126	2.8E-02	0.76	6	3E-02	
		Day 25	*0.02*	*435*	*3.8E-02*	*0.70*	*5*	3E-02	
	HLP pH 3.5	Day 2	0.02	102	2.8E-02	0.80	7	3E-02	
		Day 25	*0.02*	*88*	*1.1E-01*	*0.76*	*33*	3E-02	
300 ppb O_2	NACE A	Day 2	0.02	134	2.5E-02	0.77	5	2E-02	
		Day 25	*0.02*	*97*	*1E-01*	*0.80*	*64*	*2E-02*	
	NACE B	Day 2	0.02	122	4E-02	0.75	8	2E-02	
		Day 25	0.02	55	2E-01	0.83	90	2E-02	
	HLP pH 3.5	Day 2	0.02	110	3E-02	0.77	6	3E-02	
		Day 25	0.02	58	2E-01	0.81	73	3E-02	

Table 4 Comparisons of mass-loss corrosion rates and integrated electrochemical corrosion rates (EIS CR) of X65 samples after exposure to O_2-free and O_2-contaminated buffer solutions (T = 24°C, P_{H2S} ~100 kPa) for a period of ~30 days.

	NACE A	NACEA +O_2	NACE B	NACE B + O_2	HLP	HLP+O_2
Mass loss (µm/y)	740 (±40)	1900 (±100)	1140 (±60)	2760 (±120)	2450 (±30)	3040 (±120)
EIS CR (µm/y)	820	1600	1180	2550	2200	2730

Table 5: Important periods during H-permeation testing for X65 steel exposed to O_2-free and O_2-polluted buffer solutions (T = 24°C, P_{H2S} ~100 kPa over 25 – 30 days exposure). Unbuffered 3.5% NaCl data are included (from Deffo *et al*) [12] to serve as a comparison.

	j_{peak} ($\mu A\ cm^{-2}$) *(after 1-2h)*	j_{ss} ($\mu A\ cm^{-2}$) *(day 5 -15)*	j_{final} ($\mu A\ cm^{-2}$))	*Percent decrease from j_{ss}*
NACE A	155	51 (± 3)	2	96%
NACE A + O_2	130	54 (± 2)	47	13%
NACE B	200	54 (± 3)	6	89%
NACE B + O_2	190	59 (± 2)	48	19%
HLP	225	50 (± 3)	30	40 %
HLP + O_2	235	60 (± 2)	51	16%
Unbuffered 3.5% NaCl	*56 (± 4)*	*44 (± 2)*	*40*	*9%*

Table 6: XRD phase IDs in (descending order of dominance) from the X65 corrosion/hydrogen permeation membrane surfaces after 30 days immersion in 100 kPa H_2S-saturated buffer solutions held at 24°C for a period of 30 days, in descending order of dominance.

	$[O_2]_{aq}$ < 10 ppb	$[O_2]_{aq}$ = 300 ppb
NACE A	troilite	*troilite, mackinawite*
NACE B	troilite, Fe	*troilite, pyrite, Fe*
HLP pH 3.5	troilite, mackinawite	*troilite, pyrite, pyrrhotite, marcasite*

Corrosion and hydrogen permeation in H_2S environments with O_2 contamination – Part 3: the impact of acetate-buffered test solution chemistry

Gaurav R. Joshi, ‡* Martien Duvall Deffo Ayagou,** C. Mendibide,** Thi Tuyet Mai Tran,*** Bernard Tribollet*** and Jean Kittel

‡Corresponding author: Gaurav R. Joshi (Gauroba@gmail.com)

* IFP Energies Nouvelles, Rond-point de l'échangeur de Solaize BP3, Solaize, F-69360 (FRANCE)

** Institut de la Corrosion Site de Saint-Etienne, ZA du parc secteur Gampille, Fraisses, F-42490 (FRANCE)

*** Sorbonne Université, CNRS, Laboratoire Interfaces et Systèmes Electrochimiques (LISE), Paris F-75005 (FRANCE)

This paper highlights the importance of considering the magnitude of acetate (ethanoate) species concentration on corrosion and hydrogen permeation rates, important factors associated with cracking initiation in steels for sour service qualification. Materials selection relies on standards, such as NACE TM0177 and NACE TM0284, which stipulate that oxygen pollution should be avoided during testing in H_2S-containing media. The 5% NaCl test solutions in current standards are buffered using acetic acid (CH_3COOH)/sodium acetate (CH_3COONa) to fix the solution pH over long periods. In this third paper, as part of a series of articles that evaluate how oxygen entry modifies the corrosion of (and hydrogen permeation across) low alloy steel membranes in H_2S-containing solutions, we investigate the effect that changing the solution chemistry has through testing X65 steel in different concentrations of acetic acid and sodium acetate in H_2S-saturated 5% NaCl solutions, i.e. Solutions A and B (NACE TM0177-2016), and the HLP solution of NACE TM 0284-2016. Increasing the total acetic acid + acetate concentration encourages a higher average X65 corrosion rate and longer-sustained hydrogen charging flux, assigned to the cathodic reaction rate enhancement by acetic acid and the iron solubilizing effects of acetates. Introducing 300 ppb of dissolved oxygen does not push the solution pH outside of the permitted error range but increases average X65 corrosion rates and, again, helps sustain hydrogen permeation flux for longer. Through an evaluation of the surface structure and electrochemical impedance spectroscopy data, this appears to be down to an increase in the permeability and porosity of the troilite $FeS_{troilite}$ dominant scale. The HLP solution (at pH 3.5), with the highest acetic acid and acetate concentration, is the most aggressive. In this electrolyte, an iron sulfide overlayer structure is attained with an oxygen-rich inner layer between the metal substrate and a thick iron sulfide film.

Figures

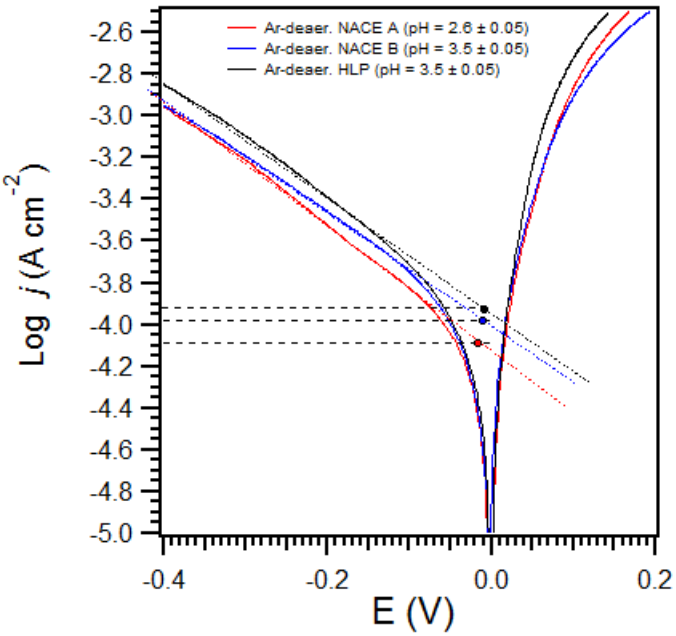

FIGURE 1: Log *j*-E potentiodynamic polarisation (PDP) curves of pure Fe exposed to Ar-deaerated buffer solutions at T = 24°C, plotted as Log *j* vs. overpotential for comparison purposes. The Ecorr values are listed in Table 2.

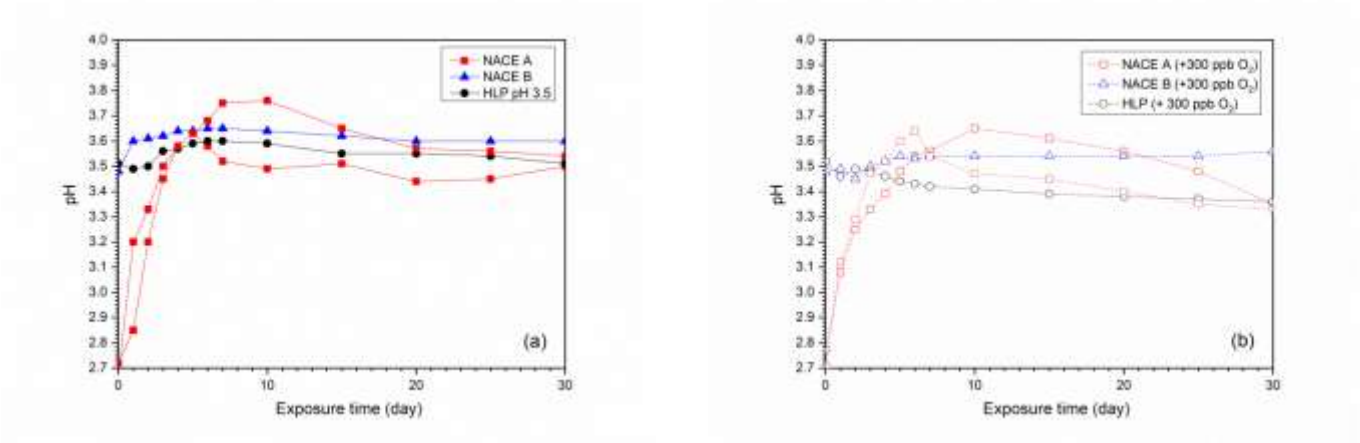

FIGURE 2: Evolution of test solution pH as a function of time over 30 days (T = 24°C, P_{H2S} = 100 kPa), (a) without and (b) with O_2 contamination.

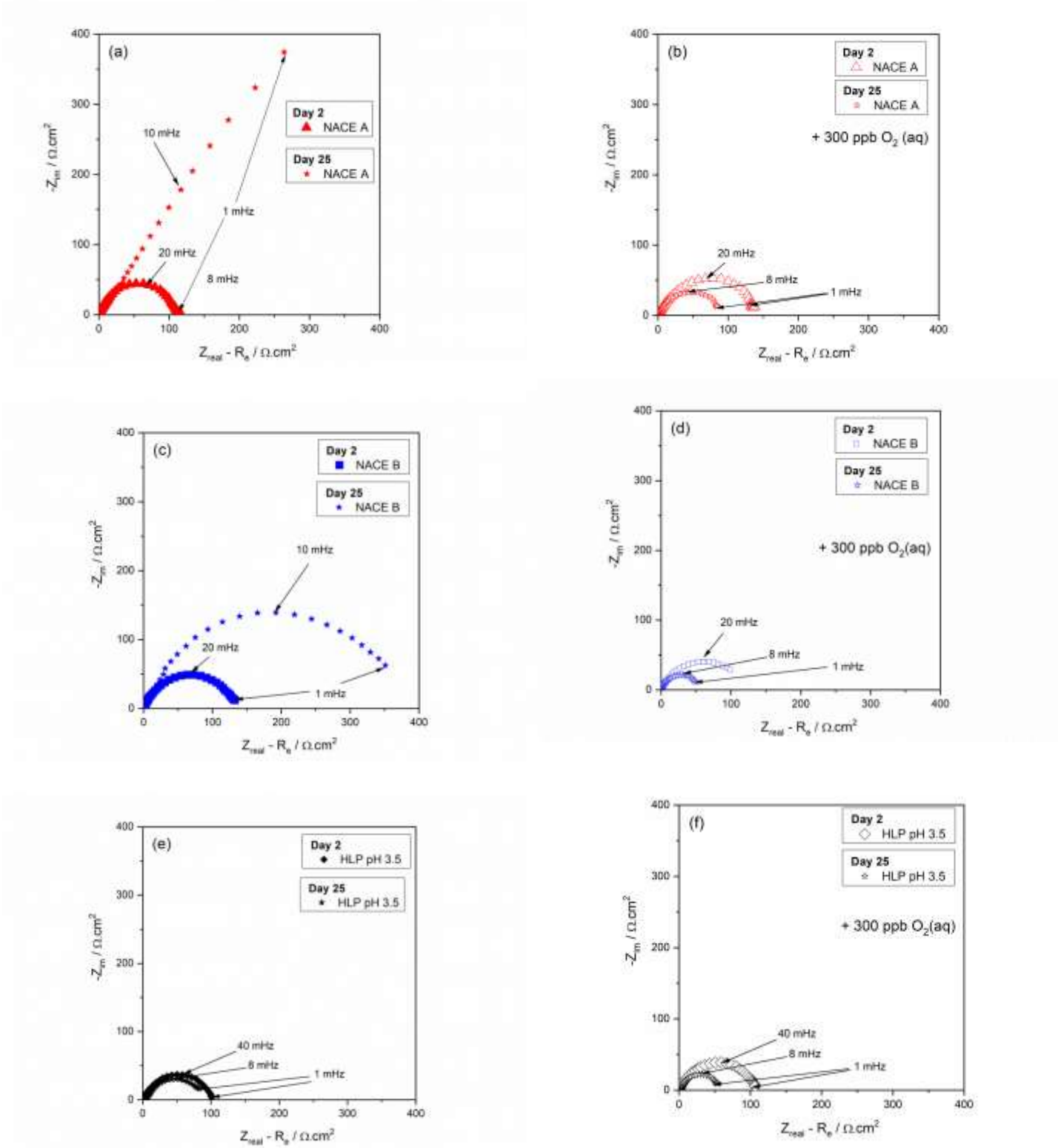

FIGURE 3: EIS diagrams of X65 membrane at various exposure times of after 2 days and 25 days of exposure, without and with O_2 contamination ($[O_2]_{aq}$ = 300 ppb) in (a-b) NACE A (c-d) NACE B and (e-f) HLP pH 3.5 buffer solutions held at T = 24°C under 100 kPa H_2S.

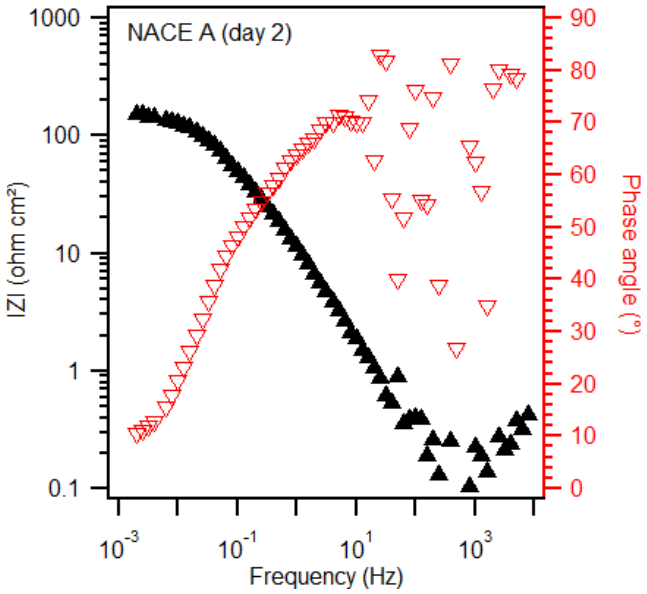

FIGURE 4: EIS diagram (Bode / Phase angle plot) of X65 membrane after 2 days exposure, without O_2 contamination, in NACE A buffer solutions held at T = 24°C under 100 kPa H_2S.

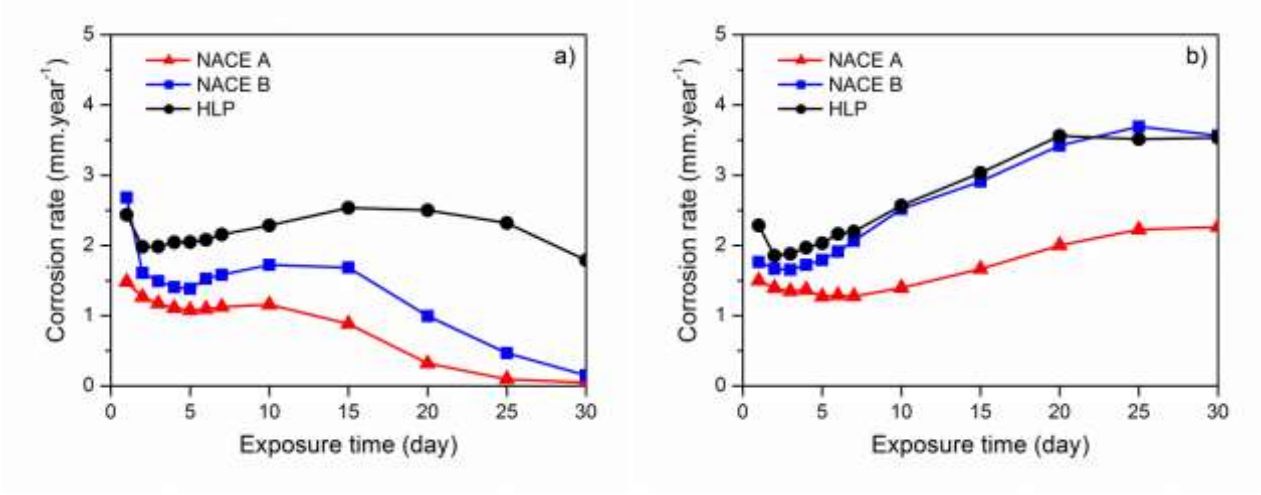

FIGURE 5: Electrochemical corrosion rates of X65 membrane exposed to buffer solutions at T = 24°C under 100 kPa H_2S (a) without and (b) with deliberate O_2 contamination ($[O_2]_{aq}$ = 300 ppb).

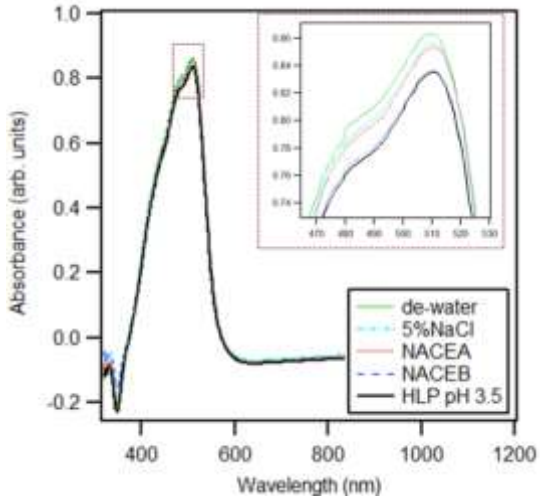

FIGURE 6: uV-Vis spectral curves of absorbance vs. wavelength for dissolved iron (from $FeSO_4$), 4.93 x 10^{-5} ml/L, in solutions containing different concentrations of acetic acid + sodium acetate. A magnified inset is included in the top right around the peak absorbance centered at λ = 510 nm.

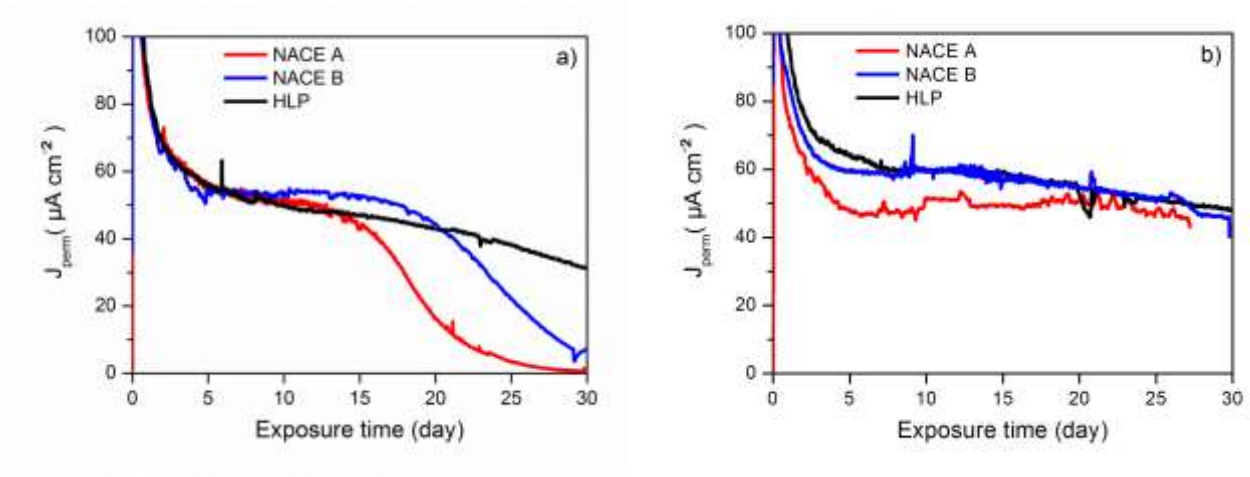

FIGURE 7: Hydrogen permeation across X65 membrane exposed to buffer solutions at T = 24°C under 100 kPa H_2S (a) without and (b) with deliberate O_2 contamination ($[O_2]_{aq}$ = 300 ppb).

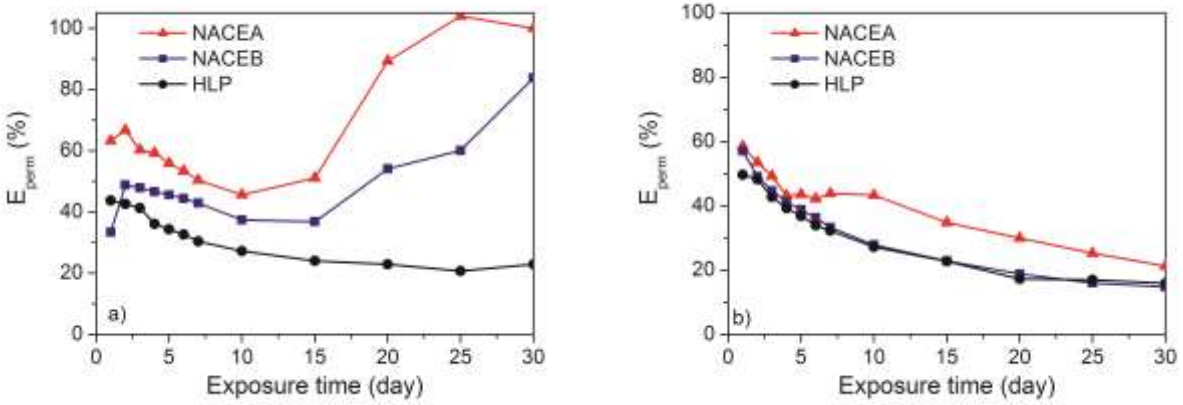

FIGURE 8: Permeation efficiencies across X65 membrane exposed to buffer solutions at T = 24°C under 100 kPa H2S (a) without and (b) with deliberate O2 contamination ($[O_2]_{aq}$=300 ppb).

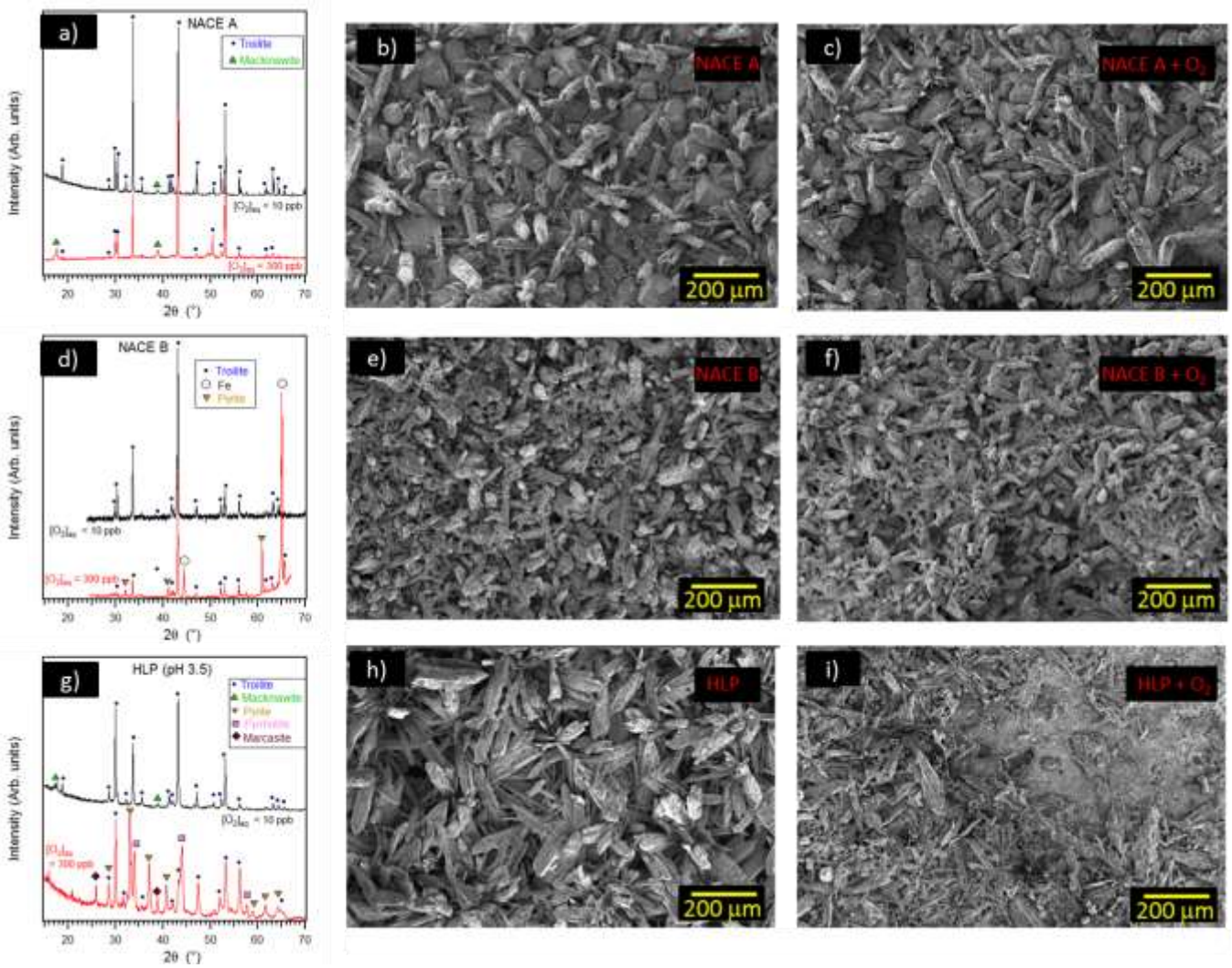

Fig. 9: XRD diffractograms and surface SEM images of X65 membranes exposed to 100 kPa H_2S-saturated (a-c) NACE A, (d-f) NACE B and (g-i) HLP buffer solutions held at 24°C for a period of 30 days. In the XRD plots, the O_2-free (black) and O_2-contaminated (red) diffractograms are presented offset.

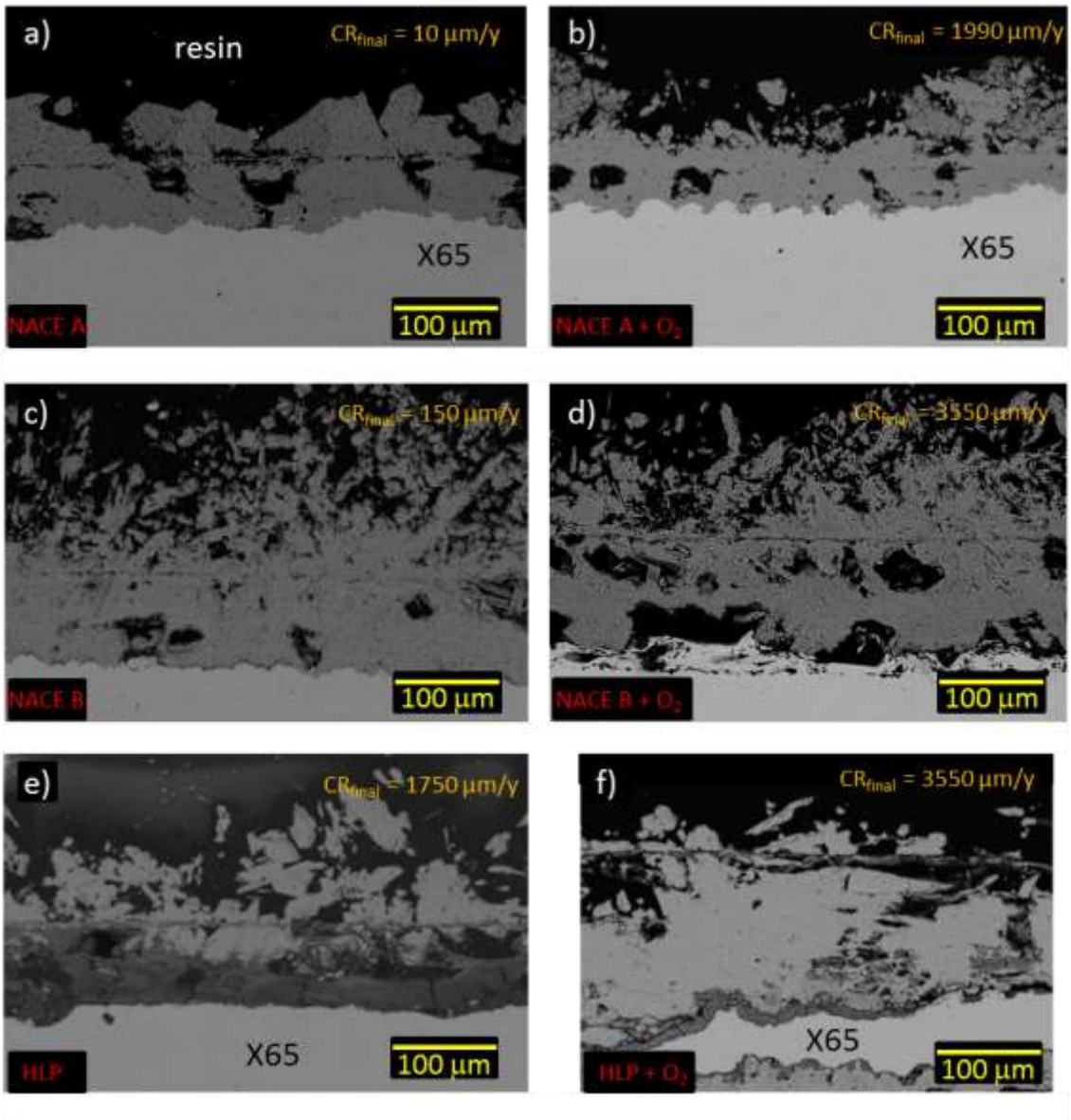

Figure 10: Cross-sectional SEM images of X65 membranes exposed to 100 kPa H_2S-saturated (a-b) NACE A, (c-d) NACE B and (e-f) HLP pH 3.5 buffer solutions held at 24°C for a period of 30 days, with and without continuous O_2 contamination ($[O_2]_{aq}$ = 300 ppb).

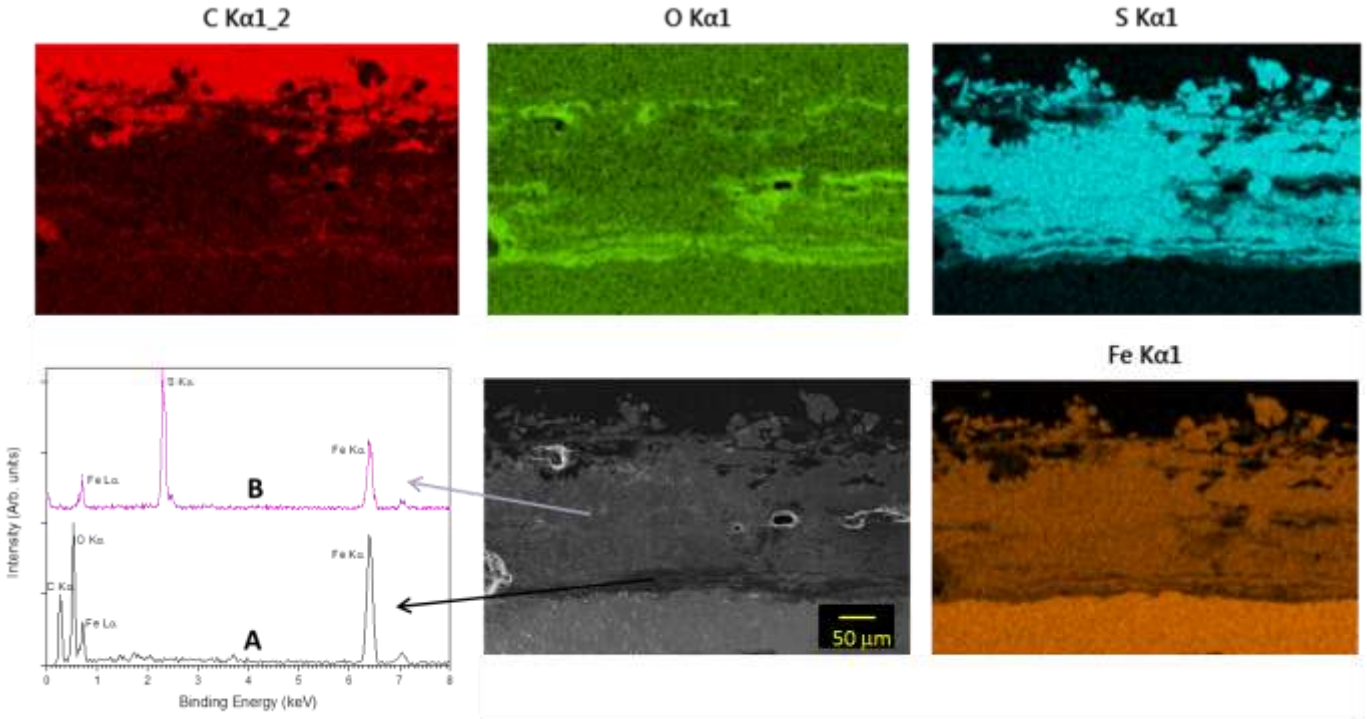

Fig. 11: SEM-EDS mapping of a cross-section of X65 exposed to 100 kPa H_2S-saturated HLP buffer solution with continuous O_2 contamination (300 ppb) held at 24°C for a period of 30 days.

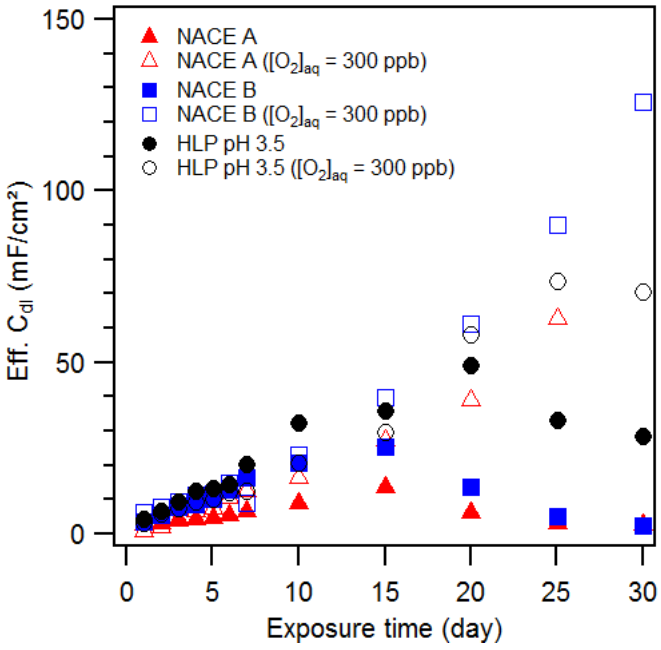

Figure 12: Eff. C_{dl} evolution of X65 surface exposed to the buffer solutions at T = 24°C under 100 kPa H_2S over 30 days with and without O_2 contamination at ($[O_2]_{aq}$ = 300 ppb).